nature communications

Article

https://doi.org/10.1038/s41467-024-55370-z

High-purity hydrogen production from dehydrogenation of methylcyclohexane catalyzed by zeolite-encapsulated subnanometer platinum-iron clusters

Received: 20 May 2024

Accepted: 9 December 2024

Published online: 02 January 2025

Check for updates

Zhe He[1,6], Kailang Li[2,3,6], Tianxiang Chen[4,6], Yunchao Feng[1], Eduardo Villalobos-Portillo[5], Carlo Marini[5], Tsz Woon Benedict Lo[4] ✉, Fuyuan Yang[3] ✉, Liang Zhang[2,3] ✉ & Lichen Liu[1] ✉

Liquid organic hydrogen carriers (LOHCs) are considered promising carriers for large-scale H_2 storage and transportation, among which the toluene-methylcyclohexane cycle has attracted great attention from industry and academia because of the low cost and its compatibility with the current infrastructure facility for the transportation of chemicals. The large-scale deployment of the H_2 storage/transportation plants based on the toluene-methylcyclohexane cycle relies on the use of high-performance catalysts, especially for the H_2 release process through the dehydrogenation of methylcyclohexane. In this work, we have developed a highly efficient catalyst for MCH dehydrogenation reaction by incorporating subnanometer PtFe clusters with precisely controlled composition and location within a rigid zeolite matrix. The resultant zeolite-encapsulated PtFe clusters exhibit the up-to-date highest reaction rate for dehydrogenation of methylcyclohexane to toluene, very high chemoselectivity to toluene (enabling the production of H_2 with purity >99.9%), remarkably high stability (>2000 h) and regenerability over consecutive reaction-regeneration cycles.

With the explosive production of green hydrogen from water electrolyzers based on renewable energy resources, the large-scale storage and transportation of hydrogen are vital for building a sustainable society based on hydrogen energy[1,2]. Among the alternative strategies, H_2 storage based on liquid organic hydrogen carriers (LOHC) is considered a promising route for large-scale implementation due to its compatibility with current industry infrastructure[3–6]. To date, several LOHC-based hydrogen storage systems have been proposed, among which the hydrogenation-dehydrogenation cycle between toluene (TOL) and methylcyclohexane (MCH) has attracted tremendous attention from academia and industry[7,8]. As shown in Fig. 1a, the combination of water electrolysis, synthesis of TOL from fossil resources or hydrogenation of captured CO_2, and the H_2 storage process based on the MCH-TOL cycle can establish a sustainable production chain in the generation and transportation of green H_2 and aromatic resources, which strongly relies on the development of efficient catalysts in each step.

From the mechanistic point of view, the dehydrogenation of MCH to TOL could be a critical step in the H_2 storage system based on the

---

[1] Engineering Research Center of Advanced Rare-Earth Materials of Ministry of Education, Department of Chemistry, Tsinghua University, Beijing, China. [2] Center for Combustion Energy, Tsinghua University, Beijing, China. [3] School of Vehicle and Mobility, Tsinghua University, Beijing, China. [4] Department of Applied Biology and Chemical Technology, The Hong Kong Polytechnic University, Hunghom, Hong Kong, China. [5] ALBA Synchrotron Light Source, Cerdanyola del Vallès, Barcelona, Spain. [6] These authors contributed equally: Zhe He, Kailang Li, Tianxiang Chen. ✉e-mail: benedict.tw.lo@polyu.edu.hk; fyyang@tsinghua.edu.cn; zhangbright@tsinghua.edu.cn; lichenliu@mail.tsinghua.edu.cn

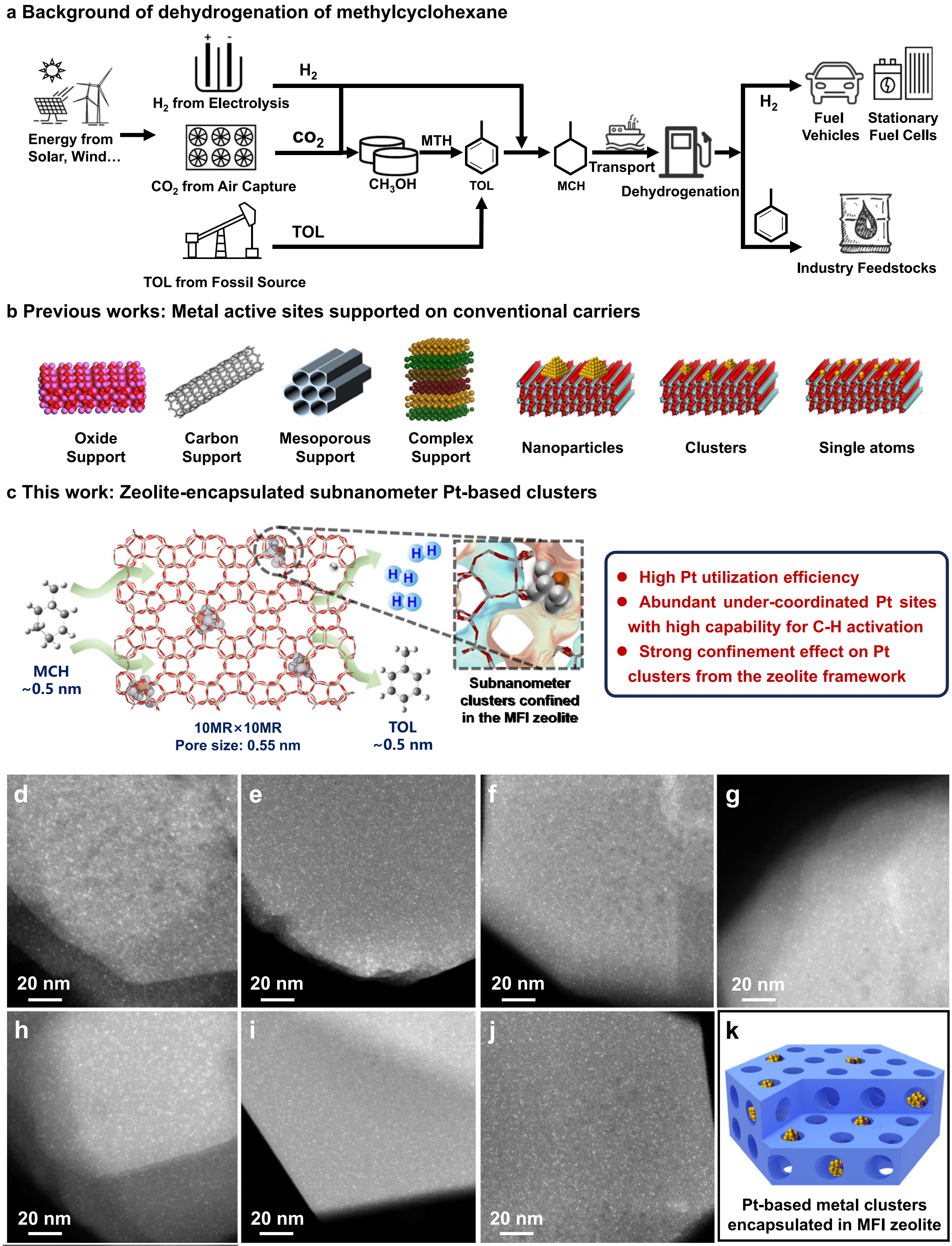

Fig. 1 | Solid catalysts for H_2 storage and transportation based on toluene-methylcyclohexane cycle. a A sustainable production chain in the generation and transportation of green H_2 and aromatic resources. Green H_2 is generated from water electrolysis based on renewable electricity and green toluene is produced from fossil resources or hydrogenation of CO_2 from direct air capture. The green toluene can further serve as the carrier for H_2 through hydrogenation of toluene to MCH and then transport to the target market. At the endpoint, H_2 is released through the MCH dehydrogenation reaction, and the resultant toluene can be further used in the chemical industry for downstream processes. **b** Illustrations of the structural features of the supported metal catalysts for MCH dehydrogenation reaction. **c** Structural features of the zeolite-encapsulated bimetallic PtFe clusters developed in this work for MCH dehydrogenation reaction. **d**–**k** HAADF-STEM image of the Pt@MFI and $PtM_{4.7}$@MFI catalysts. **d** $PtZn_{4.7}$@MFI, (**e**) $PtSn_{4.7}$@MFI, (**f**) $PtMn_{4.7}$@MFI, (**g**) $PtFe_{4.7}$@MFI, (**h**) $PtGa_{4.7}$@MFI, (**i**) $PtIn_{4.7}$@MFI, (**j**) Pt@MFI. **k** Schematic illustration of the Pt-based zeolite materials, in which subnanometer Pt clusters are encapsulated within the MFI zeolite crystallites.

MCH-TOL cycle, because the dehydrogenation of MCH is an endothermic process and relies on the activation of *sp*^{3}-type C-H bonds[9]. From a practical point of view, the solid catalysts need to deal with concentrated MCH feeds to achieve high efficiency in H_2 production. Besides, considering the inevitable deactivation of supported metal catalysts under dehydrogenation reaction conditions due to coke formation, the catalyst must show robust recyclability in consecutive reaction-regeneration cycles. Moreover, the purity of H_2 produced from the dehydrogenation of LOHC is an essential criterion for evaluating the catalyst's potential for storing H_2 for fuel cells, thus requiring the deployment of a highly selective catalyst for the dehydrogenation process[10]. As illustrated in Fig. 1b, although numerous strategies have been proposed for improving the performances of supported metal catalysts for MCH dehydrogenation, such as optimization of metal-support synergy, and modifying the chemical composition and domain size of the metal active sites[11–15]. For instance, by selectively poisoning the Pt nanoparticles supported on Al_2O_3 by sulfur, high activity, and selectivity have been achieved in the MCH dehydrogenation reaction and the S-modified Pt/Al_2O_3 catalysts are now being used in the commercial process[16,17]. To further decrease the cost of the supported Pt catalysts and reduce the reactor size, it is of interest to develop efficient Pt catalysts with high specific activities in H_2 production from MCH dehydrogenation reaction.

In this work, we have developed a highly efficient supported Pt catalyst for MCH dehydrogenation reaction by incorporating subnanometer bimetallic PtFe clusters with precisely controlled composition and location within a zeolite matrix (Fig. 1c). The rigid zeolite framework can provide effective confinement on the subnanometer PtFe clusters to suppress the sintering of the active sites during the MCH dehydrogenation reaction[18]. The resultant zeolite-encapsulated PtFe clusters exhibit the up-to-date highest reaction rate for MCH dehydrogenation reaction, very high chemoselectivity to toluene (enabling the production of H_2 with purity >99.9%), remarkably high stability (>2000 h) and regenerability over consecutive reaction-regeneration cycles.

Results

Synthesis of Pt-based catalysts

Pure-silica MFI-type zeolite with three-dimensional pore structures is chosen as the host for subnanometer metal species because the pore dimensions of the 10-member ring (10MR) channels well match the molecule size of TOL and MCH (see illustration in Fig. 1c). We anticipate that, if the active Pt sites can be well stabilized in the 10MR channels of MFI zeolite, the MCH can diffuse along the zeolite channels to access the Pt sites for catalytic transformation into toluene, but the mobility of the active Pt sites will be constrained by the rigid zeolite channels, resulting in a highly stable catalyst[19,20]. Following this hypothesis, we have prepared a series of Pt@MFI and bimetallic $PtM_{4.7}$@MFI (M = Sn, Zn, Ga, In and Fe) materials one-pot synthesis with an M/Pt molar ratio of ~4.7 (see illustrative description of the synthesis process in Supplementary Fig. 1), which allows the simultaneous encapsulation of subnanometer Pt and M species into the zeolite crystallites during the crystallization process without affecting the formation of MFI zeolite crystallites (see field emission scanning electron microscopy images and XRD patterns in Supplementary Figs. 2–9). The M elements are involved in tuning the electronic properties of Pt species and then modulating the catalytic properties[21,22].

As shown in Fig. 1 and Supplementary Figs. 10–16, subnanometer Pt clusters with an average particle size of ~0.6 nm are formed within the MFI zeolite crystallites in the monometallic Pt@MFI sample, which remain stable after calcination in air and reduction by H_2 at 600 °C. Furthermore, the encapsulations of subnanometer PtM clusters into the MFI zeolite crystallites are also validated with the $PtM_{4.7}$@MFI materials, indicating that introducing M elements does not affect the generation and size distributions of Pt clusters.

We have employed the high-resolution scanning transmission electron microscopy (STEM) imaging technique to figure out the exact location of the Pt clusters in the microporous zeolite matrix. As shown in Fig. 2 and Supplementary Figs. 17–30, by correlating the paired high-angle annular dark-field (HAADF-STEM) image and the integrated differential phase contrast (iDPC-STEM) image, the Pt clusters are determined to be predominantly in the sinusoidal 10MR channels of MFI zeolite structure, regardless of the type of the M elements[23]. The above characterization results infer that the $PtM_{4.7}$@MFI materials can be employed as model systems to study the influences of the chemical composition of subnanometer Pt-based catalysts for MCH dehydrogenation, which may provide new insights into the structure-reactivity relationship in the subnanometer regime.

Evaluation of the Pt-based catalysts for MCH dehydrogenation

The catalytic performances of the Pt-based catalysts have been tested for MCH dehydrogenation reaction in a fix-bed reactor at ambient pressure. As shown in Fig. 3a, b, the monometallic Pt@MFI sample shows nearly complete conversion of MCH at 350 °C at WHSV of 2.2 h^{-1} when using mixture of MCH and N_2 (MCH:N_2 = 1:1) as the reaction feed and the Pt@MFI catalyst remains stable for >60 h and gives 97–99% selectivity to TOL over the testing period, suggesting that subnanometer Pt clusters are highly active for MCH dehydrogenation reaction, which could be associated with the advantages of the under-coordinated Pt sites in Pt clusters for activation of saturated C-H bonds in MCH[24].

As suggested by Fig. 3a, b, the addition of M species into the Pt@MFI material has remarkable impacts on the catalytic properties. In the cases of $PtZn_{4.7}$@MFI, $PtGa_{4.7}$@MFI, and $PtIn_{4.7}$@MFI, they exhibit significantly declined activities for MCH dehydrogenation. Morphological and spectroscopy characterization of the spent catalysts infer that the low initial reaction rates and rapid catalyst deactivation of $PtZn_{4.7}$@MFI, $PtGa_{4.7}$@MFI, and $PtIn_{4.7}$@MFI catalysts could be related to the modification of the electronic properties of Pt clusters by the co-catalyst metal species, resulting in low capability for C-H activation and elevated coke deposition (Supplementary Figs. 31–35). In contrast, the $PtSn_{4.7}$@MFI and PtFe@MFI show similar activity as the Pt@MFI catalyst over the course of ~20 h. More importantly, under steady reaction conditions, the $PtSn_{4.7}$@MFI and $PtFe_{4.7}$@MFI show improved selectivity to toluene (~99%), indicating that introducing Sn and Fe can suppress the undesired conversion of toluene to benzene. The short induction period observed with the $PtFe_{4.7}$@MFI catalyst could be associated with the covering of the residual acid sites by the coke species as indicated by the NH_3 temperature-programmed desorption (NH_3-TPD) profiles (Supplementary Figs. 36). The long-term catalytic tests show that the $PtSn_{4.7}$@MFI catalyst suffers deactivation after ~20 h on stream (Fig. 3c, d). In comparison, the $PtFe_{4.7}$@MFI catalyst maintains a high conversion of MCH (>90%) and very high selectivity (~99%) for >85 h of time on stream, indicating the potential of $PtFe_{4.7}$@MFI as an efficient, stable, and highly selective catalyst for MCH dehydrogenation reaction. The accelerated deactivation of $PtSn_{4.7}$@MFI catalyst after reaction for ~25 h could be caused by coke deposition on the MFI zeolite crystallites, leading to a rapid loss of available Pt sites to the reactants.

It should be noted that, besides the co-catalyst metal, K^+ is also a critical promotor in the Pt-zeolite catalysts for stabilizing the subnanometer Pt clusters in MFI zeolite channels. In the absence of K^+ promotor, Pt nanoparticles are formed in the K-free $PtFe_{4.7}$@MFI catalyst and exhibit very low activity for the MCH dehydrogenation reaction (Supplementary Figs. 37–38).

Structural characterizations of the PtFe@MFI catalysts

Based on the above results, we have optimized the bimetallic $PtFe_x$@MFI catalysts by varying the Fe loading while fixing the Pt loading. Electron microscopy characterizations of a series of

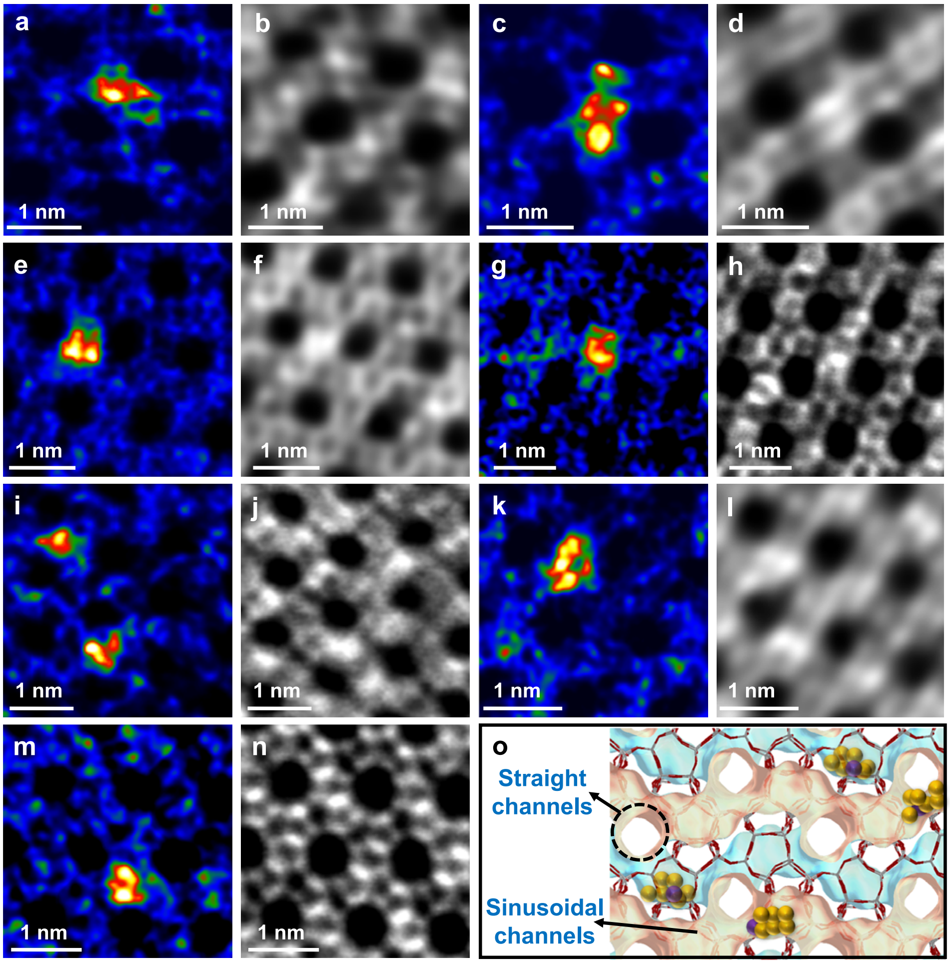

Fig. 2 | Determination of the location of subnanometer Pt clusters by electron microscopy characterization. Representative high-resolution HADDF-STEM (**a**, **c**, **e**, **g**, **i**, **k**, **m**) and the paired iDPC (**b**, **d**, **f**, **h**, **j**, **l**, **n**) images of the bimetallic $PtM_{4.7}$@MFI (**a**–**l**) and the monometallic Pt@MFI (**m**, **n**) catalysts. $PtZn_{4.7}$@MFI (**a**, **b**), $PtSn_{4.7}$@MFI (**c**, **d**), $PtMn_{4.7}$@MFI (**e**, **f**), $PtFe_{4.7}$@MFI (**g**, **h**), $PtGa_{4.7}$@MFI (**i**, **j**), $PtIn_{4.7}$@MFI (**k**, **l**). All the samples were pre-reduced by H_2 at 600 °C. **o** Schematic illustration showing the presence of subnanometric Pt clusters in the sinusoidal channels of MFI zeolite. In the HAADF-STEM images, the red and yellow colors represent the contrast of Pt clusters while the blue color represents the contrast of zeolite support.

PtFe@MFI catalysts show that adding an excess amount of Fe species as a promotor will cause the sintering of Pt species into large nanoparticles in the $PtFe_{7.9}$@MFI catalyst (Fig. 4a), which can cause a dramatic decrease in activity for MCH dehydrogenation reaction. For the $PtFe_x$@MFI (x = 0.6–4.7) samples with Fe loadings of <0.6 wt%, the morphology of the $PtFe_x$@MFI samples, size distributions, and dispersion of the Pt species and their locations within the MFI zeolite structure are quite similar (Supplementary Figs. 39–53, Fig. 4b–n and Supplementary Table 4), indicating that introducing an appropriate amount of Fe species will not affect the generation and stabilization of subnanometer Pt clusters in MFI zeolite.

To decipher the atomic-level structural features of the bimetallic PtFe species in different samples, we have employed in situ X-ray absorption spectroscopy to study the chemical states and coordination environment of Pt and Fe species in the working $PtFe_x$@MFI catalysts. As shown in Fig. 5a, the Pt L_3-edge X-ray absorption near-edge structure (XANES) spectra show the presence of metallic Pt in all the measured Pt-zeolite materials, regardless of their chemical composition, being consistent with the XPS results (Supplementary Fig. 54). The fitting results of the Pt L_3-edge extended X-ray absorption fine structure (EXAFS) spectra (Fig. 5c, Supplementary Fig. 55, and Table 1) indicate the formation of subnanometer Pt clusters in the monometallic Pt@MFI and the $PtFe_x$@MFI (x = 0.6–4.7) samples while the formation of Pt nanoparticles (>2 nm) is validated with the $PtFe_{7.9}$@MFI sample[25]. It should be noted that when the Fe loading is <0.6 wt%, only minor differences in the coordination number of Pt-Pt bonding are observed with the Pt@MFI and $PtFe_x$@MFI samples, which is consistent with the electron microscopy characterization results. The low contribution of Pt-Fe bonding in the Pt L_3-edge EXAFS spectra could be caused by the relatively low percentage of Fe species in the bimetallic PtFe clusters[26].

The comparison of the Fe K-edge XANES spectra (Fig. 5b) and those of the reference samples (Fe, FeO, Fe_2O_3 and Fe_3O_4) indicate the formation of reduced FeO_x species in the PtFe@MFI samples after the in situ reduction treatment by H_2 at 600 °C. Interestingly, the K-edge XANES spectra of the PtFe@MFI samples don't resemble any of the reference samples, inferring the presence of a mixture of different types of Fe species, which is reasonable for Fe-containing zeolite materials because of the low reducibility of Fe species encapsulated in zeolites[27,28]. Only the first-shell Fe-O bonding is observed in the Fe K-edge EXAFS spectra (Fig. 5d, Supplementary Fig. 55, and Table 1), regardless of the Fe loading in the $PtFe_x$@MFI samples, implying the presence of highly dispersed FeO_x species in the form of atomically dispersed Fe species or partially reduced FeO_x clusters in the zeolite matrices, as confirmed by the EDS mapping results (Supplementary Fig. 56)[29]. The chemical states and coordination environment of Fe

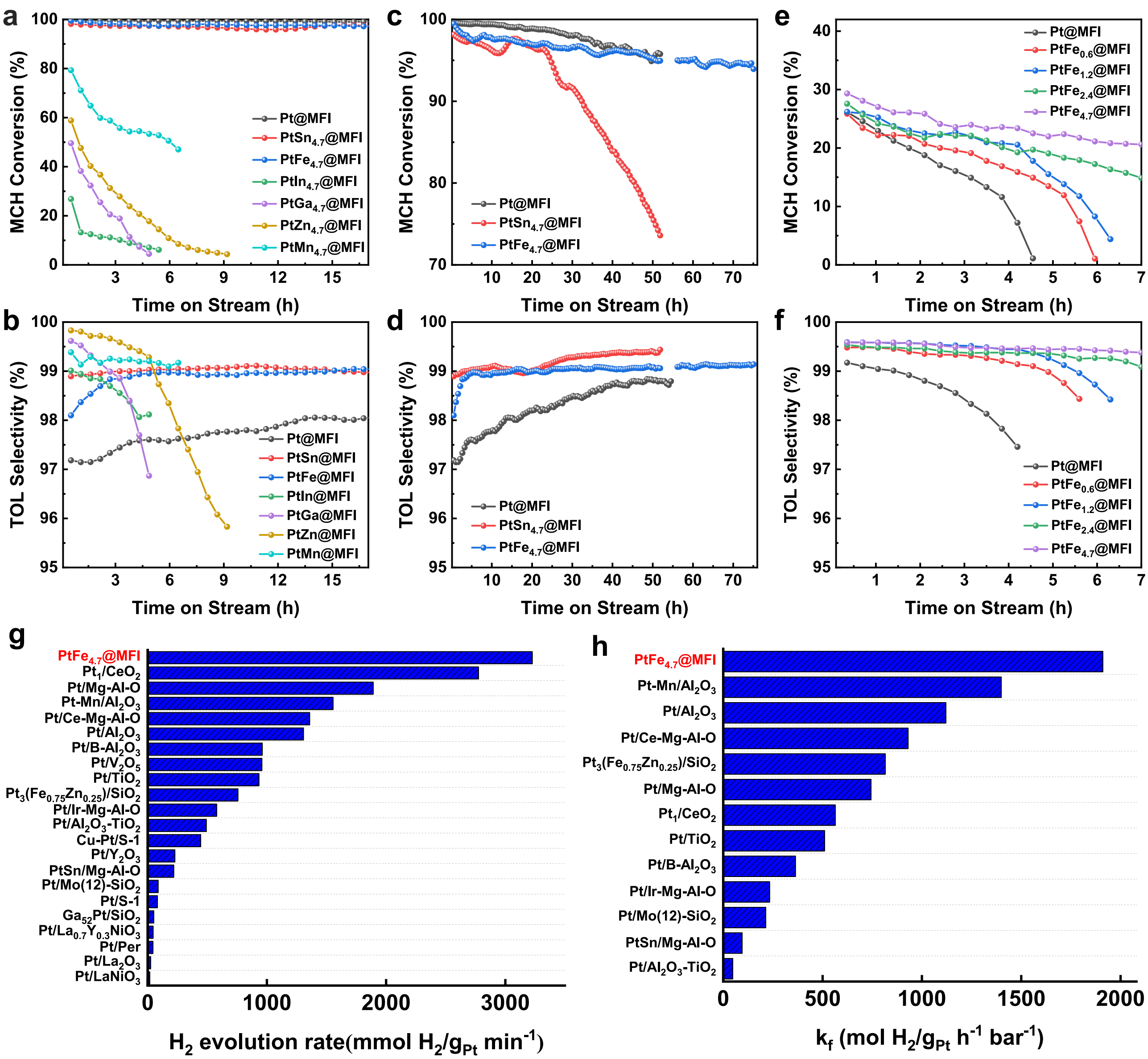

Fig. 3 | Catalytic results of Pt-zeolite materials for MCH dehydrogenation reaction. **a**, **b** MCH conversion levels and selectivity to toluene (TOL) over test periods of ~17 h of Pt@MFI and $PtM_{4.7}$@MFI (M=Sn, Zn, In, Ga, Fe) catalysts. **c**, **d** Catalytic performances of the Pt@MFI, $PtSn_{4.7}$@MFI and $PtFe_{4.7}$@MFI catalysts for extended periods of >50 h. Reaction conditions for tests shown in (**a**–**d**): 350 °C, a mixture of MCH and N_2 (MCH:N_2 = 1:1) as the feed gas, weight-hour space velocity (WHSV) = 2.2 h^{-1}. **e**, **f** Catalytic performance of Pt@MFI and $PtFe_x$@MFI (x = 4.7, 2.4, 1.2, 0.6) catalysts for MCH dehydrogenation reaction under harsh conditions. **e** MCH conversion and **f** TOL selectivity. Reaction conditions: 400 °C, a mixture of MCH and N_2 (MCH:N_2 = 1:1) as the feed gas, weight-hour space velocity (WHSV) = 108 h^{-1}. **g** Summary of the specific H_2 evolution rate of $PtFe_{4.7}$@MFI and other reported Pt-based catalysts at 350 °C. **h** Summary of the forward reaction rates (k_f) of $PtFe_{4.7}$@MFI and other reported Pt-based catalysts at 350 °C.

species are further studied by quasi in situ Mössbauer spectroscopy[30]. As summarized in Fig. 5e–h and Supplementary Table 5, regardless of the composition of the $PtFe_x$@MFI catalysts, the iron species mostly exist as iron oxide species in a combination of tetrahedrally coordinated FeO_x species (FeO_x-Tetra) and hexagonally coordinated FeO_x species (FeO_x-Hexa), which is in line with the measurement results of the magnetic properties (Supplementary Fig. 57). Besides the FeO_x species, we have also observed the presence of partially reduced Fe species in the Mössbauer spectra, which can be associated with the FeO_x ($x < 1$) clusters in the MFI zeolite channels and the reduced Fe species interacting with Pt clusters (i.e., the FePt bimetallic species). The abundances of the partially reduced Fe species in the $PtFe_{4.7}$@MFI and $PtFe_{7.9}$@MFI samples are considerably higher than that in the $PtFe_{2.4}$@MFI, which is consistent with the chemical composition analysis of the bimetallic clusters/nanoparticles by electron microscopy (Supplementary Fig. 58–59 and Supplementary Tables 6-7) and the UV-vis spectroscopy measurements (Supplementary Fig. 60–61)[27,31]. It should be noted that the absence of the FeC_x species in the bimetallic PtFe@MFI catalysts is confirmed by the Mössbauer spectra of the spent catalysts (Supplementary Fig. 62a). The incorporation of Fe into Pt clusters will cause the modification of their electronic properties, as inferred by the IR spectra using CO as the probe molecules (Supplementary Fig. 63), which can influence the adsorption/interaction between the Pt active sites and the reactant/product.

We have followed the reduction process of the pristine $PtFe_{4.7}$@MFI sample obtained from one-pot synthesis by in situ XAS to gain further insights into the formation mechanism of subnanometer PtFe clusters. As shown in Supplementary Figs. 64–65, the pristine $PtFe_{4.7}$@MFI sample (named as $PtFe_{4.7}$@MFI-air) mainly comprises oxidized Pt and Fe species. After reduction treatment by H_2 at 200 °C,

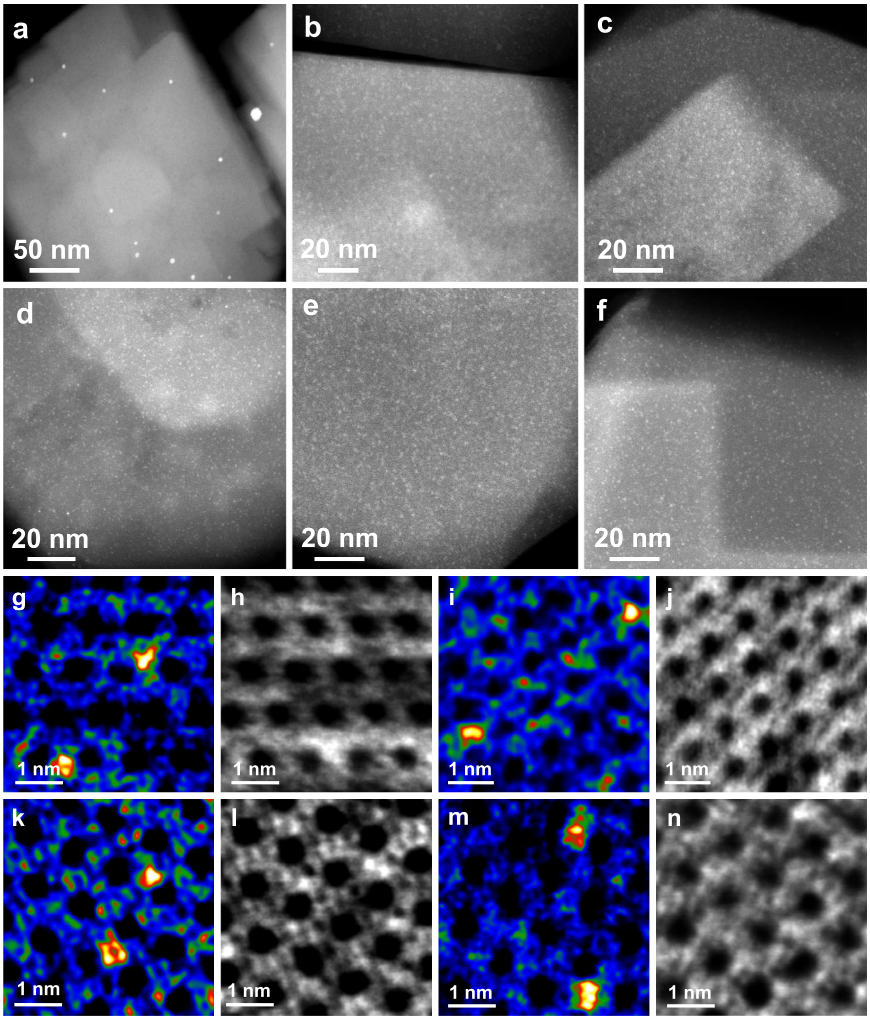

Fig. 4 | Electron microscopy characterization of PtFe$_x$@MFI catalysts with different compositions. Representative low-magnification HAADF-STEM images of the PtFe$_x$@MFI catalysts. **a** PtFe$_{7.9}$@MFI, **b** PtFe$_{4.7}$@MFI, **c** PtFe$_{2.4}$@MFI, **d** PtFe$_{1.2}$@MFI, **e** PtFe$_{0.6}$@MFI and **f** Pt@MFI. **g**–**n** Determination of the location of subnanometer Pt species in MFI zeolite structure by paired HAADF-STEM and iDPC-STEM images. Representative high-resolution HADDF-STEM (**g**, **i**, **k**, **m**) and the corresponding iDPC (**h**, **j**, **l**, **n**) images of the PtFe$_x$@MFI. **g**, **h** PtFe$_{4.7}$@MFI, **i**, **j** PtFe$_{2.4}$@MFI, **k**, **l** PtFe$_{1.2}$@MFI and **m**, **n** PtFe$_{0.6}$@MFI. In the HAADF-STEM images, the red and yellow colors represent the contrast of Pt clusters while the blue color represents the contrast of zeolite support.

we can observe the presence of Pt-Pt bonding in the Pt L$_3$-edge EXFAS spectra, indicating the formation of metallic Pt clusters, as also confirmed by HAADF-STEM images (Supplementary Figs. 66–72). After reduction treatment at 350 °C (i.e., the reaction temperature for MCH dehydrogenation), both Pt-Fe and Pt-Pt bonding are observed. This result also infers that, even if the catalyst is pre-reduced at 200 °C by H$_2$, the Pt-Fe bonding will still form in the working catalyst for the MCH dehydrogenation reaction at 350 °C. Further increasing the reduction treatment temperature to 600 °C will cause a slight increase in the coordination number of Pt-Fe bonding while the coordination number of Pt-Pt bond remains almost unchanged. The evolution behaviors of the Fe and Pt species during the catalyst activation procedure are also followed by other spectroscopy and electron microscopy techniques, which confirm the gradual formation of bimetallic PtFe clusters when elevating the reduction temperature (Supplementary Figs. 62b, 73–74 and Supplementary Table 8).

Catalytic performances of PtFe@MFI catalysts

As shown in Fig. 3e, f, when measuring the catalytic performances at 400 °C and a very high WHSV of 108 h^{-1} for better differentiating the catalysts, the monometallic Pt@MFI catalyst suffers a fast deactivation under this condition, which is probably caused by the aggravated coke deposition according to the characterizations of the spent catalyst (Supplementary Figs. 75–80). When the Fe loading is increased, the stability of the PtFe$_x$@MFI catalyst is gradually improved. With a Fe loading of 0.58 wt% (corresponding to a Fe/Pt molar ratio of 4.7), the PtFe$_{4.7}$@MFI exhibits excellent stability with a prolonged decay rate in the MCH conversion level. However, introducing an excess amount of Fe will cause sharply decreased reactivity, resulting in the loss of activity of the PtFe$_{7.9}$@MFI sample when testing at very high WHSV. The deactivation constants derived from the activity profiles show that, by incorporating an appropriate amount of Fe, the deactivation rate of the Pt@MFI catalyst can be decreased by four times (Supplementary Fig. 81).

Kinetic studies show that the bimetallic PtFe$_{4.7}$@MFI catalyst gives a lower apparent activation energy than the Pt@MFI catalyst (Supplementary Fig. 82), implying that the MCH dehydrogenation reaction is more favorable on PtFe clusters than on Pt clusters. The intrinsic reaction rates on various Pt-zeolite catalysts also infer the advantages of the bimetallic PtFe clusters over the monometallic Pt. For the bimetallic PtFe@MFI catalysts with Fe/Pt ratios ranging from 0.55 to 4.7, the more Fe the catalyst contains, the higher H$_2$ evolution rates it can achieve in the MCH dehydrogenation reaction. In particular, the optimal PtFe$_{4.7}$@MFI catalyst gives twice the H$_2$ formation rate

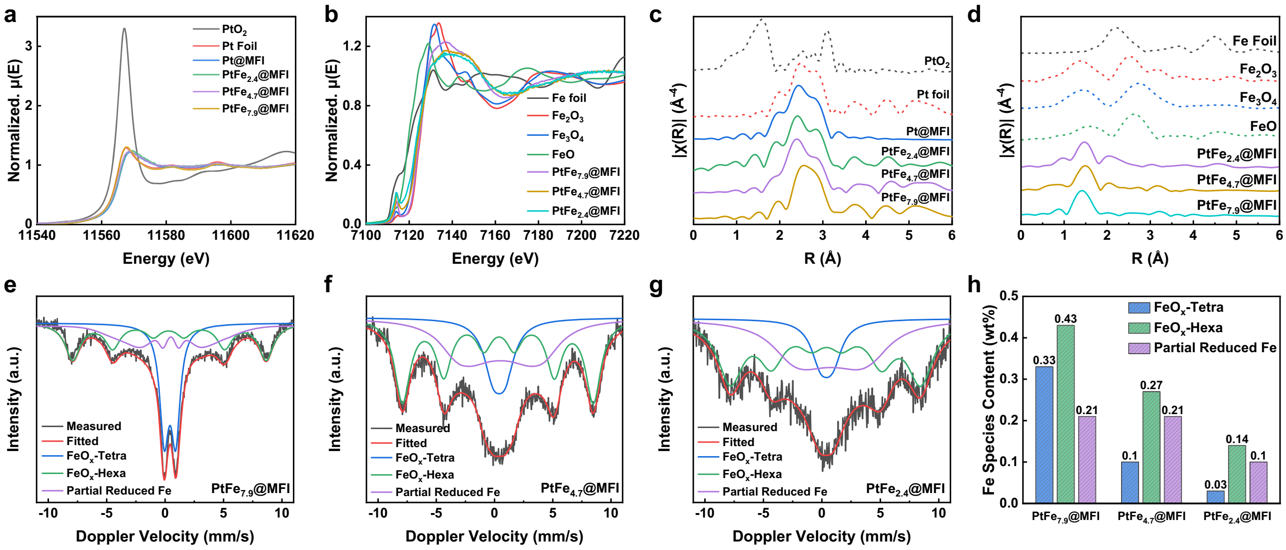

Fig. 5 | Spectroscopy characterizations of the Pt-zeolite materials. **a**–**d** Characterization results of the Pt-zeolite materials by in situ X-ray absorption spectroscopy. **a** Pt L_3-edge XANES spectra, **b** Fe K-edge XANES spectra, **c** Pt L_3-edge EXAFS spectra, **d** Fe K-edge EXAFS spectra. **e**, **f** Characterization results of the Pt-zeolite materials by in situ Mössbauer spectroscopy. **e** $PtFe_{7.9}$@MFI, **f** $PtFe_{4.7}$@MFI and **g** $PtFe_{2.4}$@MFI. The three samples were subjected to in situ reduction treatment by H_2 at 600 °C for 3 h before the collection of the Mössbauer spectra. **h** Contents of different types of Fe species in three bimetallic PtFe@MFI catalysts derived from the fitting of quasi in situ Mössbauer spectra. The contents of tetrahedrally coordinated FeO_x species (FeO_x-Tetra), hexagonally coordinated FeO_x species (FeO_x-Hexa) and Fe species in partial reduced Fe are listed in (**h**).

compared to the monometallic Pt@MFI catalyst (Supplementary Fig. 83). The comparisons between the $PtFe_{4.7}$@MFI catalyst and supported PtFe catalysts prepared by other methods confirm the superior performance of the subnanometer PtFe clusters confined in MFI zeolite generated by one-pot synthesis (Supplementary Fig. 84). The exceptional performance of the $PtFe_{4.7}$@MFI catalyst is further confirmed compared to reported Pt-based catalysts regarding the specific H_2 evolution rate (Fig. 3g and Supplementary Table 9).

Considering that the H_2 evolution rate in the MCH dehydrogenation reaction strongly depends on the reaction conditions, we have carried out the thermodynamic analysis and calculations of the forward reaction rates (k_f) based on the data provided in the literature (see detailed discussion in Supplementary Note 1). The comparative analysis suggests that the $PtFe_{4.7}$@MFI catalyst developed in this work exhibits the best performance among the reported materials to date (Fig. 3h). A detailed analysis of the gaseous by-products formed in the MCH dehydrogenation reaction shows that methane is the major component with a concentration at ~500 ppm with the $PtFe_{4.7}$@MFI catalyst, corresponding to an H_2 purity of ~99.95%, which is much lower than the Pt-based catalysts supported on oxide carriers (Supplementary Fig. 85).

Theoretical studies on the Pt-based catalysts

By collective analysis of the characterization results from different techniques, we can conclude that, Pt-Fe bonding is formed in the bimetallic $PtFe_x$@MFI samples after reduction treatment at ≥350 °C by H_2 and the abundance of the Pt-Fe bonding depends on the Fe loading. We have employed theoretical modeling and calculations to gain insights into the structure-reactivity relationship in the bimetallic PtFe@MFI samples. Initially, we constructed three models to study the influence of the chemical composition of the Pt-based active sites on the MCH dehydrogenation reaction. Three Pt-based cluster models (Pt_7, Pt_6Sn and Pt_6Fe) made by metal clusters located in the sinusoidal 10-ring channels of MFI zeolite are constructed based on the electron microscopy characterization results to represent the Pt@MFI, $PtSn_{4.7}$@MFI and $PtFe_{4.7}$@MFI catalyst, respectively. As shown in Fig. 6a and Supplementary Fig. 86, DFT-calculated O affinity shows that both Pt_7 and Pt_6Sn clusters in the Pt_7-MFI and Pt_6Sn-MFI models tend to form metallic clusters while the Fe species tend to exist in the form of Fe(II) in the Pt_6FeO-MFI model. The results of theoretical modeling align with the spectroscopic characterization results on the chemical states of Pt and Fe species in the realistic $PtFe_{4.7}$@MFI catalysts.

In light of the prior works on theoretical modeling of the MCH dehydrogenation process on metal catalysts, we have studied two plausible key steps in the transformation process from MCH to TOL (Supplementary Figs. 87–88)[9]. As shown in Fig. 6b, the Pt_6FeO clusters give lower energy barriers for activation of the C-H bonds in methylcyclohexene and methylcyclohexadiene than the Pt_7 and Pt_6Sn clusters, suggesting the high activity of Pt_6FeO clusters for MCH dehydrogenation reaction, which are in line with the experimental results from the kinetic studies. The advantages of Pt_6FeO clusters over the Pt_7 clusters in the activation of C-H bonds are further validated by the isotopic exchange experiments (Supplementary Fig. 89).

Prior mechanistic studies suggest that the coke deposition on the Pt catalyst and the production of methane due to hydrogenolysis of TOL can be associated with the undesired side reactions of TOL on the Pt active sites, which are responsible for the catalyst deactivation and decline in selectivity[32]. In this context, we have studied two elementary steps associated with the coke deposition (cleavage of the C-H bond in the methyl group of TOL) and side reaction (cleavage of the C-C bond in TOL) with the three models by DFT calculations[33]. As presented in Fig. 6c and Supplementary Figs. 90–91, the Pt_7-MFI and Pt_6Sn-MFI models exhibit similar activation energy for the two elementary steps, while the Pt_6FeO-MFI model exhibits considerably higher activation energies, inferring that the undesired elementary reactions are not favorable on bimetallic PtFe clusters. Furthermore, the adsorption of toluene and $^*C_6H_5$-CH_2 species (the coke precursor) is significantly weakened (Fig. 6d and Supplementary Fig. 92), indicating that Fe modification promotes toluene desorption and inhibits its deep dehydrogenation to produce the coke precursor, which is consistent with the activation energy analysis[34,35]. Detailed analysis of the electronic structures of the three Pt-based clusters indicates that the charge transfer from the Pt atom to the adsorbed TOL molecule at the binding site will be partly decreased on Pt_6FeO-MFI model (Supplementary Fig. 93), resulting in a relatively weaker bonding interaction of TOL on the Pt_6FeO cluster in compared to the Pt_7 and Pt_6Sn cluster, as

Table 1 | Fit results for the Pt L_3-edge and Fe K-edge EXAFS spectra of PtFe-zeolite materials

Sample	Path	C.N.	R(Å)	σ^2 (Å^2)	ΔE_0 (eV)	R_{factor}
Pt foil	Pt-Pt	12	2.767 ± 0.002	0.0044 ± 0.0002	7.5 ± 0.4	0.007
Pt@MFI	Pt-Pt	7.3 ± 0.5	2.735 ± 0.005	0.0102 ± 0.0006	6.8 ± 0.6	0.018
$PtFe_{2.4}$@MFI	Pt-O	0.8 ± 0.2	1.828 ± 0.038	0.0150 ± 0.0011	5.2 ± 0.5	0.017
	Pt-Pt	6.2 + 0.1	2.740 ± 0.005	0.0095 ± 0.0006		
$PtFe_{4.7}$@MFI	Pt-Fe	0.8 ± 0.3	2.633 ± 0.030	0.0123 ± 0.0005	5.0 ± 0.5	0.014
	Pt-Pt	6.2 ± 0.6	2.743 ± 0.004	0.0077 + 0.0004		
$PtFe_{7.9}$@MFI	Pt-Pt	8.8 ± 0.1	2.761 ± 0.001	0.0049 ± 0.0001	6.7 ± 0.1	0.001
Fe_2O_3	Fe-O	6	1.973 ± 0.007	0.0129 ± 0.0012	−9.5 ± 0.5	0.009
Fe_3O_4	Fe-O	6	1.961 ± 0.007	0.0147 ± 0.0014	−9.5 ± 0.5	0.009
$PtFe_{2.4}$@MFI	Fe-O	2.6 ± 0.1	1.850 ± 0.005	0.0017 ± 0.0008	1.7 ± 0.5	0.013
$PtFe_{4.7}$@MFI	Fe-O	2.8 ± 0.1	1.840 ± 0.003	0.0011 ± 0.0004	0.3 ± 0.3	0.004
$PtFe_{7.9}$@MFI	Fe-O	3.3 ± 0.1	1.843 ± 0.002	0.0032 ± 0.0003	−1.7 ± 0.2	0.003

C.N.: coordination numbers, R: bonding distance, σ^2: Debye-Waler factor, ΔE_0: inner potential correction, and R_{factor}: difference between modeled and experimental data. The fits of the Pt edge were performed on the first two shells (R = 1.6–3.0 Å) over the Fourier transform (FT) of the k^3-weighted $\chi(k)$ functions in the k range of 3–12 Å^{-1}. The ΔE_0 values of two Pt–O and Pt–Pt/Fe shells are constrained to share the same value in the fitting models. The many-body amplitude reduction factor s_0^2 was set as 0.9. The fits of the Fe edge were performed on the first shell (R = 1.0–2.0 Å) over the Fourier transform (FT) of the k^3-weighted $\chi(k)$ functions in the k range of 3–13 Å^{-1}. The many-body amplitude reduction factor s_0^2 was set as 0.89.

evidenced in the crystal orbital Hamilton populations (COHP) analysis (Fig. 6d, e). Consequently, the undesired transformation of TOL on Pt active sites is suppressed on the Pt_6FeO cluster (Supplementary Fig. 94).

Our experimental results show that the Fe loading and the chemical states of Fe species have marked impacts on the catalytic properties of the bimetallic $PtFe_x$@MFI catalysts (Supplementary Figs. 95–98). We have then studied the two elementary reactions on three different PtFe cluster models (Supplementary Fig. 99), and the results show that the incorporation of two Fe(II) atoms into the Pt clusters will cause a decrease in the energy barrier for C-H activation in TOL, which may accelerate the coke deposition on Pt sites. The results from DFT calculations are consistent with our experimental observation, in which we have found that the $PtFe_{7.9}$@MFI catalyst with a high Fe loading exhibits fast deactivation in the MCH dehydrogenation reaction. The combination of experimental and theoretical study demonstrates that the catalytic properties of subnanometer metal clusters are sensitive to chemical composition. Therefore, it is of great necessity to control the size and composition of the bimetallic clusters precisely[21,36,37].

Long-term stability tests

Long-term stability is a crucial criterion for the potential industrial implementation of the PtFe@MFI catalyst in the practical process. We first tested the stability of the optimized $PtFe_{4.7}$@MFI catalyst under the conditions in which the conversion levels of MCH are maintained at high levels (>90%). As shown in Fig. 7a, the optimized $PtFe_{4.7}$@MFI catalyst exhibits high activity and selectivity to TOL for >200 h in every single catalytic run. Moreover, the catalyst can be facilely regenerated by calcination in air and subsequent reduction by H_2 during a course of >2000 h in eight consecutive reaction-regeneration cycles. Furthermore, to confirm the full recovery of the regenerated PtFe@MFI catalyst, we have carried out consecutive reaction-regeneration tests under high WHSV conditions (i.e., maintaining the conversion levels <40%) which can better reflect the catalytic efficiency of the Pt active sites than the tests performed at high conversion levels. As shown in Fig. 7b, the activity of the deactivated PtFe@MFI catalyst can be fully recovered after calcination treatment in the air for the removal of the coke. Besides, even after elevating the calcination temperature to 600 °C, the performance of the PtFe@MFI catalyst will not be affected. Instead, the high-temperature calcination is helpful for the removal of hard coke on the spent catalyst, facilitating the recovery of the activity for MCH dehydrogenation reaction. After seven consecutive reaction-regeneration cycles for >400 h, the PtFe@MFI catalyst maintains its catalytic performance as the fresh catalyst. Structural characterizations of the spent catalysts show that the size distributions and location of the bimetallic PtFe clusters within the zeolite structure are retained after the long-term stability tests (Fig. 7c, j and Supplementary Figs. 100–107), suggesting the remarkably high activity and structural robustness of the subnanometer PtFe clusters confined in MFI zeolite (see the comparison with reported catalysts for MCH dehydrogenation reaction in Supplementary Table 9).

Discussion

In this work, we have reported a zeolite-encapsulated subnanometer PtFe catalyst for the production of high-purity H_2 from an MCH dehydrogenation reaction, which gives high activity, selectivity and stability under challenging reaction conditions. The remarkable performance is ascribed to the unique structures of the bimetallic PtFe clusters and the surrounding rigid zeolite framework. The principles for catalyst design can be extended to other H_2 storage systems based on other LOHCs (e.g., benzyltoluene and dibenzyltoluene) in which the size, composition and surrounding environment of the metal active sites within the microporous supports should be further optimized according to the molecular structures of the LOHC molecules and reaction mechanisms.

Methods

Chemicals

$Zn(NO_3)_2 \cdot 6H_2O$ (Aladdin, product code: Z190758-500g), $Ga(NO_3)_2 \cdot 9H_2O$ (Macklin, product code: G810494-1g), $Mn(NO_3)_2 \cdot 4H_2O$ (Energy Chemical, product code: E060921), $In(NO_3)_2 \cdot 4H_2O$ (Macklin, product code: I834112-25g), $SnCl_4 \cdot 5H_2O$ (Energy Chemical, product code: E010541), $Fe(NO_3)_3 \cdot 9H_2O$ (from Macklin, product code: I809398-100g), KCl (Sinopharm Chemical Reagent, product code: 10016318), H_2PtCl_6 (Adamas-beta, product code: 32606 A), Tetraethyl orthosilicate (TEOS, from Alfa Aesar, product code: 014082), Tetrapropylammonium hydroxide (TPAOH, 40 wt%, Energy Chemical, product code: 17456.22), Ethylenediamine (Alfa Aesar, product code: A12132.AP).

Synthesis of Pt-zeolite materials

Pt@MFI and a series of bimetallic PtM@MFI samples (where M represents the second metal, M=Sn, Zn, In, Ga, Fe) were synthesized by one-pot approach. In a typical synthesis procedure of $PtFe_{4.7}$@MFI sample, a TPAOH solution was initially prepared by blending 6.12 g of a 40 wt% TPAOH solution, 0.0531 g of KCl, and 14.1 g of distilled water at

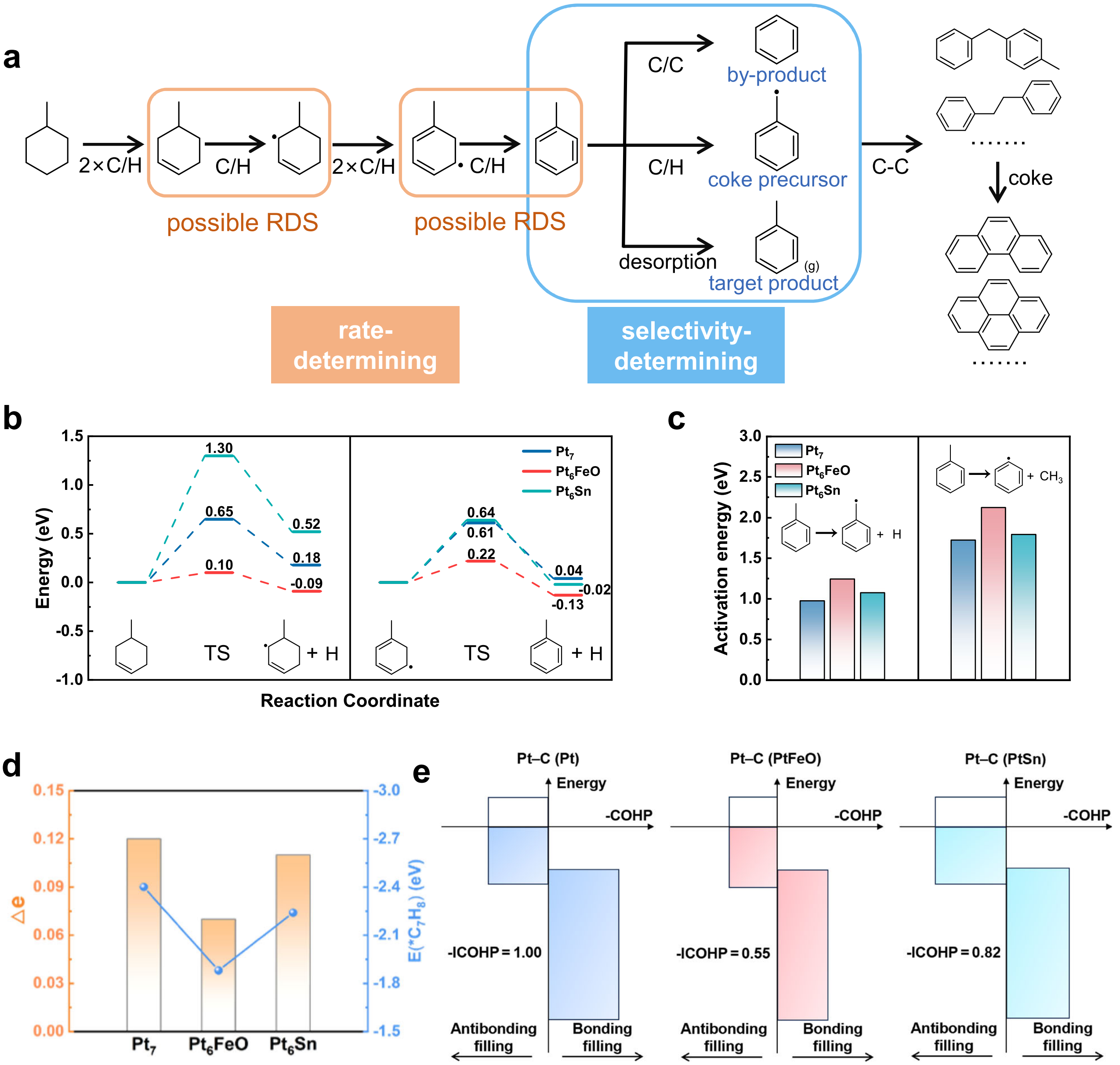

Fig. 6 | Theoretical studies on methylcyclohexane dehydrogenation over Pt-based clusters confined in MFI. a Reaction mechanism for methylcyclohexane dehydrogenation. **b** Energy profile for the third and the last steps of C-H bond cleavage of methylcyclohexane over MFI-confined Pt_7, Pt_6FeO and Pt_6Sn clusters. **c** Activation energy for C-H bond cleavage and C−C bond dissociation of toluene over MFI-confined Pt_7, Pt_6FeO and Pt_6Sn clusters. **d** Electron transfer from the top Pt site to toluene adsorbate. **e** Schematic diagram for crystal orbital Hamilton populations (COHP) analysis of Pt−C bond in toluene-adsorbed Pt_7, Pt_6FeO and Pt_6Sn clusters.

room temperature. Subsequently, 6.19 g of TEOS was added to TPAOH solution at 35 °C and then the suspension was kept stirring for 6 h to ensure the full hydrolysis of TEOS. Afterwards, 240 µL of H_2PtCl_6 aqueous solution (100 mg/mL), 87.5 mg of $Fe(NO_3)_3 \cdot 9H_2O$, and 225 µL of ethylenediamine were added to the above solution. The resulting yellow solution was then transferred to Teflon-lined autoclaves and heated in an electric oven at 175 °C for 96 h under static conditions. After the hydrothermal process, the solid product was isolated by filtration, washed with distilled water and acetone, and subsequently dried at 60 °C. The solid sample was further calcined in static air at 560 °C for 8 h with a ramp rate of 2 °C/min, followed by an additional heating step at 600 °C for 2 h with a ramp rate of 5 °C/min.

The bimetallic PtM@MFI catalysts (M = Sn, Zn, Ga, In and Fe) were prepared by altering the type of metal precursors while the M/Pt atomic ratio is maintained at around 4.7. Details of the synthesis procedure of PtM@MFI catalysts are provided in Supplementary Table 1. The preparation of the monometallic Pt@MFI sample was carried out in the absence of a co-catalyst metal precursor in the synthesis mixture. In addition, PtFe@MFI samples with different Fe loadings were prepared in a similar approach but the Fe loading was controlled by the mass of the Fe precursor added (Supplementary Table 2). The results of ICP-OES analysis of the chemical composition of Pt-based samples are shown in Supplementary Table 3.

Characterizations

Powder X-ray diffraction analysis was carried out with a Rigaku RU-200b X-ray powder diffractometer with Cu Kα radiation. Pore structure analysis was performed through argon adsorption-desorption on a BSD-660M A3M sorption instrument at −186 °C. Prior to the measurements, the reduced samples underwent a degassing process at 300 °C for 6 h. Specific surface area and micropore volume were determined using the Brunauer-Emmett-Teller (BET) and Saito-Foley

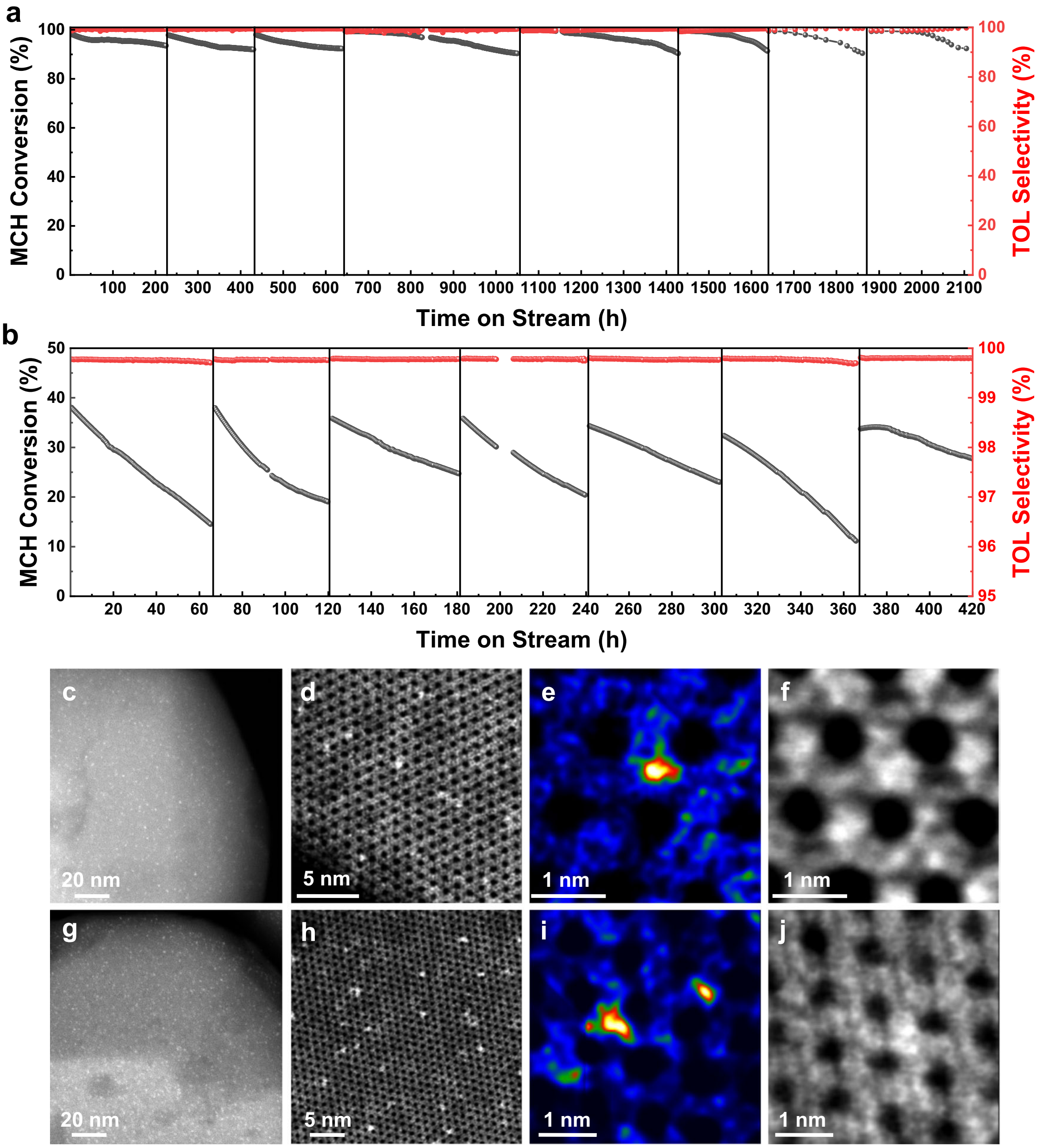

Fig. 7 | Long-term stability tests of the $PtFe_{4.7}$@MFI catalyst for MCH dehydrogenation. a Cyclic long-term catalytic experiment at high conversion levels. The conversion levels of MCH were kept above 90% to facilitate the detection of any potential activity loss after exposure to a high partial pressure of TOL. Dehydrogenation reaction conditions: 350 °C, MCH:H_2 = 1:1, WHSV = 4.4 h^{-1}. **b** Cyclic long-term catalytic experiment at high WHSV. The conversion levels of MCH were kept below 50% to facilitate the detection of any potential activity loss in the catalyst during cyclic tests. Reaction conditions: 350 °C, MCH:H_2 = 1:1, WHSV = 43 h^{-1}. In (a-b), the deactivated catalyst was subjected to a regeneration treatment by calcination in air and subsequent reduction by H_2 to restore the active sites. Structural characterizations of the spent catalyst at WHSV of 43 h^{-1} (**c**–**f**) and 4.4 h^{-1} (**g**–**j**). **c**, **d**, **g**, **h** Representative low-magnification and high-magnification of HAADF-STEM images of the spent $PtFe_{4.7}$@MFI catalysts. **e**, **f**, **i**, **j** High-resolution HAADF-STEM and the paired iDPC-STEM images of the spent $PtFe_{4.7}$@MFI catalyst, showing the presence of Pt clusters in the sinusoidal channels. In the HAADF-STEM images, the red and yellow colors represent the contrast of Pt clusters while the blue color represents the contrast of zeolite support.

(SF) models, respectively, while the total pore volume was estimated at P/P_0 = 0.99. The metal loading for all catalysts was quantified through inductively coupled plasma optical emission spectroscopy (ICP-OES) analysis using a Thermo IRIS Intrepid II instrument.

Magnetic susceptibility measurements were conducted using a Quantum Design SQUID VSM magnetometer. The measurements were conducted over a temperature range spanning from 300 K to 5 K and reciprocally from 5 K to 300 K, all under an external magnetic field of 100 Oe. To prevent oxidation, the sample was carefully placed into a pre-weighed SQUID capsule within a glovebox. Subsequently, the capsule was sealed, weighed, and transferred to the SQUID cavity for magnetic susceptibility measurements.

The quasi-in situ ^{57}Fe Mössbauer spectra were acquired at 80 K using an MFD-500AV spectrometer (Topologic Systems, Japan) with a proportional counter, utilizing ^{57}Co(Rh) as the γ-ray radioactive source. Before characterization, the sample was reduced in a 5% H_2/Ar atmosphere for 3 h at temperatures of 600 °C. After the pre-reduction treatment, the sample was carefully transferred into a capsule within a glovebox to avoid contact with air. The measuring velocity was calibrated using a standard α-iron foil. The data analysis was performed with Moss Winn 4.0i software.

UV-visible diffuse reflectance spectroscopy was performed using an ultraviolet spectrophotometer (Lambda 950) within the wavelength range of 200–800 nm. UV-Raman spectroscopic characterization was conducted at room temperature using the HORIBA JY LabRAM HR Evolution Raman spectrometer with a 266 nm excitation source.

The number of exposed metal sites in each Pt-zeolite catalyst was determined by CO pulse chemisorption experiments, which were carried out on an automatic chemisorption analyzer (BSD-Chem C200). The solid samples (100–200 mg) were subjected to pretreatment under an H_2 atmosphere at a given temperature for 3 h, followed by cooling to the adsorption temperature at ~50 °C. After purging with helium, CO pulses were injected multiple times until the cumulative quantity of adsorbed CO reached saturation. The quantity adsorbed for each CO pulse was recorded using a thermal conductivity detector, and the metal dispersion was calculated assuming a ratio of surface Pt/adsorbed CO equal to 1. The equations used for the calculation of metal dispersion (D) are provided below:

$$D(\%) = \frac{N_m F_s M \times 10^4}{L} \tag{1}$$

Where N_m represents the chemisorption uptake expressed in mol of CO per gram of the sample, and F_s represents the adsorption stoichiometry, assumed to be 1 in our measurement. M represents the molecular weight of the supported metal (Pt), and L represents the loading of Pt.

In situ CO diffuse reflectance infrared Fourier transform spectra (CO-DRIFTS) were acquired using a Bruker Tensor 27 spectrometer equipped with a mercury cadmium telluride (MCT) detector cooled by liquid nitrogen. Before the measurements, the sample was subjected to a H_2 reduction treatment at a given temperature for 3 h. Following the reduction pretreatment, the sample was exposed to 10 vol% CO/N_2 at 30 °C for 30–50 min, and the spectra were collected after purging with N_2 for an additional 30–50 min.

Samples for electron microscopy studies were prepared by dropping the suspension of the solid samples in CH_2Cl_2 directly onto holey-carbon coated copper grids. Electron Microscopy measurements were performed using two types of microscopes. A JEOL 2100 F microscope operating at 200 kV was used to record HAADF-STEM images at low resolution. High-resolution HAADF-STEM and iDPC-STEM imaging was performed on a FEI Titan[3] Themis 60–300 microscope working at 300 kV. To reduce the electron beam damage to the sample, the images were recoded with a beam current of 10–30 pA and a 2.5 µs dwell time. More details about the optimization of the measurement conditions of Pt-zeolite materials can be referred to prior work[19,38].

X-ray absorption experiments at the Pt (11,564 eV) L_{III} and Fe (7112 eV) K edges were performed in NOTOS beamline in ALBA synchrotron. The beam was monochromatized using Si(111) double crystals; harmonic rejection was performed setting the correct angle of collimating and focusing mirrors. Si and Rh stripes have been chosen to adjust the reflectivity curves. The spectra were collected in fluorescence modes by means of the ionization chambers filled with appropriate gases (95% N_2 + 5% Kr for I_0 (ionization chamber 0, located before the sample) and 17.1% N_2 + 82.9% Kr for I_1 (ionization chamber 1, located after the sample)), and a fluorescence solid-state detector. Samples was diluted using BN and loaded inside a high-pressure gas cell with one end of the both-way open-ended quartz capillary (diameter of 1 mm) is connected to desired gas, and the other end is connected to the mass spectrometer for on-line gas analysis. Several scans were acquired at each measurement step to ensure spectral reproducibility and good signal-to-noise ratio. The data reduction and extraction of the $\chi(k)$ function were performed using the Athena code. EXAFS data analysis was performed using the Artemis software. Phase and amplitudes were calculated with the FEFF6 code.

Theoretical calculations

Density functional theory calculations were completed via Vienna ab initio simulation software package with the atomic simulation environment[39,40]. As a form of the generalized gradient approximation, the Perdew–Burke–Ernzerhof functional was carried out to describe the electron exchange and correlation effects[41]. DFT-D3 method with Becke-Jonson damping was utilized to deal with van der Waals correction for the catalytic systems[42]. The projector-augmented wave method was used to treat the interaction between atomic cores and electrons[43]. The plane-wave basis set was employed with a cutoff energy of 400 eV. Besides, the atomic force convergence criterion was set to 0.03 eV/Å. Three Pt-based clusters (Pt_7, Pt_6Sn and Pt_6Fe) confined in MFI zeolite were constructed to represent the Pt@MFI, PtSn@MFI and PtFe@MFI catalysts, respectively. A 1 × 1 × 1 Gamma point was selected for geometry optimization. Besides, all models were fully relaxed.

To find transition state geometries, a combination of the climbing image nudged elastic band (CI-NEB) method and dimer method was employed with a total of 6 images[44,45]. There was only one imaginary frequency for all transition state structures.

The adsorption energy of the adsorbate is calculated by the following equation:

$$E(\text{*ads}) = E(\text{clean} + \text{ads}) - E(\text{clean}) - E(\text{gas}) \tag{2}$$

Where E(clean+ads) is the energy for the model after the adsorption of the adsorbate, E(clean) is the energy for the model without any adsorbate, E(gas) is the energy for the adsorbate in its gas phase.

Here, we took the energies of methylcyclohexane(g) and hydrogen(g) as references, the adsorption energy of other species was further calculated by the reference energies. Take methylbenzene as an example:

$$E\left(\text{*}C_7H_8\right) = E\left(\text{clean} + C_7H_8\right) - E(\text{clean}) - [E(C_7H_{14(g)}) - 3E(H_{2(g)})] \tag{3}$$

Where $E(\text{*}C_7H_8)$ is the adsorption energy of methylbenzene species on the model, $E(C_7H_{14(g)})$ and $E(H_2)$ are the reference energies.

The activation energy of an elementary step is calculated by the following equations:

$$E_{\text{act}} = E_{\text{TS}} - E_{\text{IS}} \tag{4}$$

Where E_{act} is the activation energy of a specific elementary step. E_{IS} and E_{TS} are initial state energy and transition state energy for the step, respectively.

Catalytic testing

For screening the candidate materials for MCH dehydrogenation reaction, the catalytic tests were conducted in a fixed-bed reactor under atmospheric pressure using a mixture of MCH/N_2 as the feed gas at 350 °C. Prior to the reaction, the PtM@MFI catalyst was pre-reduced by H_2 (5% H_2 diluted by Ar, 20 mL/min) at 600 °C for 3 h with a ramp rate of 10 °C/min. Following the reduction pre-treatment, the sample was cooled to 350 °C in a N_2 atmosphere. Subsequently, the reaction was initiated by introducing the reactant mixture ($MCH:N_2$ = 1:1). The N_2 feed was regulated by a mass flow controller, and the MCH feed was controlled using an injection pump.

When measuring the initial reaction rates, a fresh Pt-zeolite catalyst was used for each measurement at a specific temperature. By using a mixture of MCH and H_2 as the reaction feed, at the initial several hours, the Pt-zeolite catalyst remains relatively stable, allowing us to acquire a reliable initial reaction rate for calculating the specific reaction rates normalized to the total mass of Pt species in the solid zeolite or to the exposed Pt sites determined by CO chemisorption.

To investigate the apparent activation energy of a series of catalysts, the conversions of MCH were adjusted to below 25% by varying the weight-hour-space-velocity (WHSV) while the feed composition is fixed to MCH/H_2 mixture with an MCH/H_2 of 1/1. For obtaining the apparent activation energy, the yield of TOL was measured at 300, 320, 350, 380, and 400 °C.

To expedite the catalyst selection process, MCH conversion levels were adjusted the weight-hour-space-velocity (WHSV) while maintaining a constant ratio of MCH/N_2 in the feed gas. The products were analysed using an online GC (Agilent 8890 equipped with TCD and FID detectors). The conversion of MCH (X_{MCH}), selectivity of TOL (S_{TOL}), yield of TOL (Y_{TOL}), H_2 evolution rate (R_{H_2}), and the deactivation constant (k_d) were calculated based on the following Equations.

$$X_{MCH} = \frac{F_{MCH,in} - F_{MCH,out}}{F_{MCH,in}} \times 100\% \qquad (5)$$

$$S_{TOL} = \frac{F_{TOL,out}}{F_{MCH,in} - F_{MCH,out}} \times 100\% \qquad (6)$$

$$Y_{TOL} = X_{MCH} \times S_{TOL} \times 100\% \qquad (7)$$

$$R_{H_2}\left(\mathrm{mmol/g_{Pt}/min}\right) = \frac{3 \times Y_{TOL} \times F_{MCH,in}}{M_{Pt}} \qquad (8)$$

$$k_d\left(h^{-1}\right) = \frac{\ln\frac{1-X_{final}}{X_{final}} - \ln\frac{1-X_{initial}}{X_{initial}}}{t} \qquad (9)$$

where $F_{MCH,in}$ and $F_{MCH,out}$, represent the flow velocity of MCH in the feed and effluent, respectively and $F_{TOL,out}$ represents the flow velocity of TOL in the effluent; M_{Pt} represents the mass of Pt in the solid catalyst. $X_{initial}$ and X_{final} represent the initial and final conversion of MCH, respectively, and t represents the time the reaction time.

Long-term stability tests

To assess the catalyst's regeneration stability under severe deactivation conditions and working stability under high conversion conditions, the conversion levels of MCH were kept below 50% to facilitate the detection of any potential deactivation of the varying the $PtFe_{4.8}$@MFI catalyst during consecutive reaction-regeneration cycles. To simulate MCH dehydrogenation under practical working conditions, the reactant feed was changed to MCH/H_2 mixture with an MCH/H_2 of 1/1 which allows the downstream application of the H_2 released from LOHC. Before the catalytic test, the $PtFe_{4.8}$@MFI catalyst was subjected to a pre-reduction treatment by H_2 (5% H_2 diluted by Ar, 20 mL/min) at 200 °C for 3 h. Following the reduction pre-treatment, the catalytic test was initiated by introducing the reactant gas mixture (MCH:H_2 = 1:1) under atmospheric pressure at 350 °C with a WHSV of 43 h^{-1}, with a ramp rate of 10 °C/min from 200 to 350 °C. After the initial MCH dehydrogenation test, the sample was cooled to ~100 °C and initiated the regeneration process through calcination in air at 450 °C for 3 h, with a ramp rate of 2 °C/min. Following air calcination, the sample was cooled to 100 °C and then subjected to reduction with H_2 at 200 °C for 3 h. After reduction, the second cycle of the MCH dehydrogenation reaction was initiated by introducing the reactant gas mixture (MCH:H_2 = 1:1) under atmospheric pressure at 350 °C, with a ramp rate of 10 °C/min from 200 to 350 °C. The regeneration procedure for the samples after the third and fifth cycles remained consistent with the process after the first MCH dehydrogenation. However, for the regeneration of the samples after the fourth and sixth cycles of the MCH dehydrogenation reaction, the calcination temperature was increased to 600 °C, while the other regeneration procedures remained the same as for the samples after the first MCH dehydrogenation.

To evaluate the performance of the $PtFe_{4.8}$@MFI catalyst at high MCH conversion levels, the WHSV is changed to 4.3 h^{-1} at atmosphere pressure while the reaction temperature is maintained at 350 °C. The pretreatment and the regeneration procedure is the same as the stability tests performed at high WHSV.

Data availability

The data that support the findings of this study are present in the paper and/or the Supplementary Information and are available from the corresponding authors on request.

References

1. Nazir, H. et al. Is the H_2 economy realizable in the foreseeable future? Part II: H_2 storage, transportation, and distribution. *Int. J. Hydrog. Energy* **45**, 20693–20708 (2020).
2. Abdalla, A. M. et al. Hydrogen production, storage, transportation and key challenges with applications: a review. *Energy Convers. Manag.* **165**, 602–627 (2018).
3. Preuster, P., Papp, C. & Wasserscheid, P. Liquid Organic Hydrogen Carriers (LOHCs): toward a hydrogen-free hydrogen economy. *Acc. Chem. Res.* **50**, 74–85 (2016).
4. Wei, D. et al. Toward a hydrogen economy: development of heterogeneous catalysts for chemical hydrogen storage and release reactions. *ACS Energy Lett.* **7**, 3734–3752 (2022).
5. Salman, M. S., Rambhujun, N., Pratthana, C., Srivastava, K. & Aguey-Zinsou, K.-F. Catalysis in liquid organic hydrogen storage: recent advances, challenges, and perspectives. *Ind. Eng. Chem. Res.* **61**, 6067–6105 (2022).
6. Niermann, M., Timmerberg, S., Drünert, S. & Kaltschmitt, M. Liquid organic hydrogen carriers and alternatives for international transport of renewable hydrogen. *Renew. Sustain. Energy Rev.* **135**, 110171 (2021).
7. Liu, L. et al. Atomic-level understanding on the evolution behavior of subnanometric Pt and Sn species during high-temperature treatments for generation of dense PtSn clusters in zeolites. *J. Catal.* **391**, 11–24 (2020).
8. Gianotti, E., Taillades-Jacquin, M., Rozière, J. & Jones, D. J. High-purity hydrogen generation via dehydrogenation of organic carriers: a review on the catalytic process. *ACS Catal.* **8**, 4660–4680 (2018).
9. Zhao, W., Chizallet, C., Sautet, P. & Raybaud, P. Dehydrogenation mechanisms of methyl-cyclohexane on γ-Al_2O_3 supported Pt_{13}: impact of cluster ductility. *J. Catal.* **370**, 118–129 (2019).
10. Bulgarin, A., Jorschick, H., Preuster, P., Bösmann, A. & Wasserscheid, P. Purity of hydrogen released from the liquid organic hydrogen carrier compound perhydro dibenzyltoluene by catalytic dehydrogenation. *Int. J. Hydrog. Energy* **45**, 712–720 (2020).
11. Nakaya, Y., Miyazaki, M., Yamazoe, S., Shimizu, K. I. & Furukawa, S. Active, selective, and durable catalyst for alkane dehydrogenation based on a well-designed trimetallic alloy. *ACS Catal.* **10**, 5163–5172 (2020).
12. Chen, L. et al. Reversible dehydrogenation and rehydrogenation of cyclohexane and methylcyclohexane by single-site platinum catalyst. *Nat. Commun.* **13**, 1092 (2022).
13. Wang, J. et al. Size-dependent catalytic cyclohexane dehydrogenation with platinum nanoparticles on nitrogen-doped carbon. *Energy Fuels* **34**, 16542–16551 (2020).
14. Al-ShaikhAli, A. H., Jedidi, A., Anjum, D. H., Cavallo, L. & Takanabe, K. Kinetics on NiZn bimetallic catalysts for hydrogen evolution via selective dehydrogenation of methylcyclohexane to toluene. *ACS Catal.* **7**, 1592–1600 (2017).

15. Murata, K. et al. Structure–property relationships of Pt–Sn nanoparticles supported on Al_2O_3 for the dehydrogenation of methylcyclohexane. *ACS Appl. Nano Mater.* **4**, 4532–4541 (2021).
16. Yoshimi, O. et al. SPERA hydrogen systemtm by LOHC-MCH method for massive hydrogen storage and transportation. *J. Environ. Sci. Eng. A* **13**, 50–60 (2024).
17. Alhumaidan, F., Cresswell, D. & Garforth, A. Hydrogen storage in liquid organic hydride: producing hydrogen catalytically from methylcyclohexane. *Energy Fuels* **25**, 4217–4234 (2011).
18. Liu, L. & Corma, A. Confining isolated atoms and clusters in crystalline porous materials for catalysis. *Nat. Rev. Mater.* **6**, 244–263 (2020).
19. Liu, L. et al. Regioselective generation and reactivity control of subnanometric platinum clusters in zeolites for high-temperature catalysis. *Nat. Mater.* **18**, 866–873 (2019).
20. Liu, L. & Corma, A. Identification of the active sites in supported subnanometric metal catalysts. *Nat. Catal.* **4**, 453–456 (2021).
21. Liu, L. & Corma, A. Bimetallic sites for catalysis: from binuclear metal sites to bimetallic nanoclusters and nanoparticles. *Chem. Rev.* **123**, 4855–4933 (2023).
22. Nakaya, Y. & Furukawa, S. Catalysis of alloys: classification, principles, and design for a variety of materials and reactions. *Chem. Rev.* **123**, 5859–5947 (2022).
23. Liu, L., Lopez-Haro, M., Calvino, J. J. & Corma, A. Tutorial: structural characterization of isolated metal atoms and subnanometric metal clusters in zeolites. *Nat. Protoc.* **16**, 1871–1906 (2020).
24. Biswas, S. et al. Origin of regioselectivity in the dehydrogenation of alkanes by pincer–iridium complexes: a combined experimental and computational study. *ACS Catal.* **11**, 12038–12051 (2021).
25. Jentys, A. Estimation of mean size and shape of small metal particles by EXAFS. *Phys. Chem. Chem. Phys.* **1**, 4059–4063 (1999).
26. Liu, L. et al. Structural modulation and direct measurement of subnanometric bimetallic PtSn clusters confined in zeolites. *Nat. Catal.* **3**, 628–638 (2020).
27. Liu, Y. et al. Isomorphously Substituted [Fe,Al]ZSM-5 Catalysts for Methane Dehydroaromatization. *ACS Catal.* **13**, 8128–8138 (2023).
28. Boubnov, A. et al. Selective catalytic reduction of NO Over Fe-ZSM-5: mechanistic insights by Operando HERFD-XANES and Valence-to-Core X-ray emission spectroscopy. *J. Am. Chem. Soc.* **136**, 13006–13015 (2014).
29. Buttignol, F. et al. Aging of industrial Fe-zeolite based catalysts for nitrous oxide abatement in nitric acid production plants. *Catal. Sci. Technol.* **12**, 7308–7321 (2022).
30. Kornas, A., Mlekodaj, K. & Tabor, E. Nature and redox properties of iron sites in zeolites revealed by Mössbauer spectroscopy. *ChemPlusChem* **89**, e202300543 (2023).
31. Agote-Arán, M. et al. Operando HERFD-XANES/XES studies reveal differences in the activity of Fe-species in MFI and CHA structures for the standard selective catalytic reduction of NO with NH3. *Appl. Catal. A Gen.* **570**, 283–291 (2019).
32. Antunes, A. P. et al. Catalytic oxidation of toluene over CuNaHY zeolites. *Appl. Catal. B Environ.* **33**, 149–164 (2001).
33. Du, S., Gamliel, D. P., Giotto, M. V., Valla, J. A. & Bollas, G. M. Coke formation of model compounds relevant to pyrolysis bio-oil over ZSM-5. *Appl. Catal. A Gen.* **513**, 67–81 (2016).
34. Furukawa, S. et al. Remarkable enhancement in hydrogenation ability by phosphidation of ruthenium: specific surface structure having unique Ru ensembles. *ACS Catal.* **8**, 8177–8181 (2018).
35. Tsai, M. C. & Muetterties, E. L. Platinum metal surface chemistry of benzene and toluene. *J. Am. Chem. Soc.* **104**, 2534–2539 (2002).
36. Alexeev, O. S. & Gates, B. C. Supported bimetallic cluster catalysts. *Ind. Eng. Chem. Res.* **42**, 1571–1587 (2002).
37. Lavroff, R. H., Morgan, HarryW. T., Zhang, Z., Poths, P. & Alexandrova, A. N. Ensemble representation of catalytic interfaces: soloists, orchestras, and everything in-between. *Chem. Sci.* **13**, 8003–8016 (2022).
38. Liu, L., Lopez-Haro, M., Calvino, J. J. & Corma, A. Tutorial: structural characterization of isolated metal atoms and subnanometric metal clusters in zeolites. *Nat. Protoc.* **16**, 1871–1906 (2021).
39. Kresse, G. & Furthmüller, J. Efficiency of ab-initio total energy calculations for metals and semiconductors using a plane-wave basis set. *Comput. Mater. Sci.* **6**, 15–50 (1996).
40. Kresse, G. & Hafner, J. Ab initiomolecular-dynamics simulation of the liquid-metal–amorphous-semiconductor transition in germanium. *Phys. Rev. B* **49**, 14251–14269 (1994).
41. Perdew, J. P., Burke, K. & Ernzerhof, M. Generalized gradient approximation made simple. *Phys. Rev. Lett.* **77**, 3865–3868 (1996).
42. Grimme, S., Ehrlich, S. & Goerigk, L. Effect of the damping function in dispersion corrected density functional theory. *J. Comput.l Chem.* **32**, 1456–1465 (2011).
43. Kresse, G. & Joubert, D. From ultrasoft pseudopotentials to the projector augmented-wave method. *Phys. Rev. B* **59**, 1758–1775 (1999).
44. Henkelman, G. & Jónsson, H. Improved tangent estimate in the nudged elastic band method for finding minimum energy paths and saddle points. *J. Chem. Phys.* **113**, 9978–9985 (2000).
45. Henkelman, G. & Jónsson, H. A dimer method for finding saddle points on high dimensional potential surfaces using only first derivatives. *J. Chem. Phys.* **111**, 7010–7022 (1999).

Acknowledgements

This study is sponsored by Tsinghua-Toyota Joint Research Institute Inter-disciplinary Program. The in situ XAS experiments were performed at NOTOS BL16 beamline at ALBA Synchrotron with the collaboration of ALBA staff. We thank Dr. R. Zong for his help in the electron microscopy characterization of the Pt-zeolite catalysts at Tsinghua University.

Author contributions

L.L. conceived the project. L.Z. designed theoretical studies. Z.H. carried out the materials synthesis and the structural characterizations. K.L. performed the theoretical calculations. T.C. and B.T.W.L. conducted the in situ XAS measurements and analysed the data. Y.F. contributed to the STEM characterization of the Pt-zeolite materials. E.V. and C.M. contributed to the spectroscopic characterization of Pt-zeolite materials by XAS. F.Y. contributed to the analysis of the catalytic results. L.L. wrote the manuscript with input from all the other authors.

Competing interests

The authors declare no competing interests.

Additional information

Supplementary information The online version contains supplementary material available at https://doi.org/10.1038/s41467-024-55370-z.

Correspondence and requests for materials should be addressed to Tsz Woon Benedict Lo, Fuyuan Yang, Liang Zhang or Lichen Liu.

Peer review information *Nature Communications* thanks Gerhard Pirngruber and Kazuhiro Takanabe for their contribution to the peer review of this work. A peer review file is available.

Reprints and permissions information is available at http://www.nature.com/reprints

Publisher's note Springer Nature remains neutral with regard to jurisdictional claims in published maps and institutional affiliations.

Open Access This article is licensed under a Creative Commons Attribution-NonCommercial-NoDerivatives 4.0 International License, which permits any non-commercial use, sharing, distribution and reproduction in any medium or format, as long as you give appropriate credit to the original author(s) and the source, provide a link to the Creative Commons licence, and indicate if you modified the licensed material. You do not have permission under this licence to share adapted material derived from this article or parts of it. The images or other third party material in this article are included in the article's Creative Commons licence, unless indicated otherwise in a credit line to the material. If material is not included in the article's Creative Commons licence and your intended use is not permitted by statutory regulation or exceeds the permitted use, you will need to obtain permission directly from the copyright holder. To view a copy of this licence, visit http://creativecommons.org/licenses/by-nc-nd/4.0/.

© The Author(s) 2024